Knudsen number effects on the nonlinear acoustic spectral energy cascade

Shubham Thirani,* Prateek Gupta, and Carlo Scalo
School of Mechanical Engineering, Purdue University, West Lafayette, Indiana 47906, USA

(Received 18 September 2019; accepted 2 January 2020; published 3 February 2020)

We present a numerical investigation of the effects of gas rarefaction on the energy dynamics of resonating planar nonlinear acoustic waves. The problem setup is a gas-filled, adiabatic tube, excited from one end by a piston oscillating at the fundamental resonant frequency of the tube and closed at the other end; nonlinear wave steepening occurs until a limit cycle is reached, resulting in shock formation for sufficiently high densities. The Knudsen number, defined here as the ratio of the characteristic molecular collision timescale to the resonance period, is varied in the range $\mathrm{Kn} = 10^{-1}$–10^{-5}, from rarefied to dense regime, by changing the base density of the gas. The working fluid is Argon. A numerical solution of the Boltzmann equation, closed with the Bhatnagar-Gross-Krook model, is used to simulate cases for $\mathrm{Kn} \geqslant 0.01$. The fully compressible one-dimensional Navier-Stokes equations are used for $\mathrm{Kn} < 0.01$ with adaptive mesh refinement to resolve the resonating weak shocks, reaching wave Mach numbers up to 1.01. Nonlinear wave steepening and shock formation are associated with spectral broadening of the acoustic energy in the wavenumber-frequency domain; the latter is defined based on the exact energy corollary for second-order nonlinear acoustics derived by Gupta and Scalo [Phys. Rev. E **98**, 033117 (2018)], representing the Lyapunov function of the system. At the limit cycle, the acoustic energy spectra exhibit an equilibrium energy cascade with a -2 slope in the inertial range, also observed in freely decaying nonlinear acoustic waves by the same authors. In the present system, energy is introduced externally via a piston at low wavenumbers or frequencies and balanced by thermoviscous dissipation at high wavenumbers or frequencies, responsible for the base temperature increase in the system. The thermoviscous dissipation rate is shown to scale as Kn^2 for fixed Reynolds number based on the maximum velocity amplitude, i.e., increasing with the degree of flow rarefaction; consistently, the smallest length scale of the steepened waves at the limit cycle, corresponding to the thickness of the shock (when present) also increases with Kn. For a given fixed piston velocity amplitude, the bandwidth of the inertial range of the spectral energy cascade decreases with increasing Knudsen numbers, resulting in a reduced resonant response of the system. By exploiting dimensionless scaling laws borrowed by Kolmogorov's theory of hydrodynamic turbulence, it is shown that an inertial range for spectral energy transfer can be expected for acoustic Reynolds numbers $\mathrm{Re}_{U_{\max}} > 100$, based on the maximum acoustic velocity amplitude in the domain.

DOI: 10.1103/PhysRevE.101.023101

I. INTRODUCTION

Nonlinear acoustic processes are observed in various engineering applications such as harmonic resonators [1,2], thermoacoustic engines [3,4], ultrasonic imaging [5,6], and high-speed boundary layers [7,8]. An important feature of nonlinear acoustic processes is wave steepening, typically associated with thermodynamic nonlinearities [9]: regions of positive pressure fluctuations are characterized by higher temperatures and, hence, locally higher sound speeds (and vice versa); this leads to the enhancement of spatial gradients in the wave propagation speed yielding wave steepening [10]. In the spectral space, wave steepening entails energy cascade into higher harmonics, associated with the formation of progressively smaller length scales and timescales [11]. Figure 1 illustrates such an energy cascade by showing the temporal evolution of average velocity magnitude and wavenumber spectral density of a freely propagating nonlinear wave in a periodic domain. Due to generation of smaller length scales and timescales (higher wavenumber and frequency content), the thermoviscous dissipation increases, causing the total perturbation energy to decrease in time [Fig. 1(b)] but also limiting the spectral extent of the inertial cascade range [e.g., to $k \simeq 10^4$ at time $t = t_3$, in Fig. 1(c)].

For a resonant system with continuous external energy injection driven to its nonlinear limit cycle, such as the one considered in the present manuscript (Fig. 2), an equilibrium interscale energy transfer is achieved in the spectral space: the resonant energy cascades down to higher harmonics reaching progressively smaller length scales, until thermoviscous dissipation takes over, sustaining the shock thickness. The bandwidth of the thus-obtained broadened energy spectrum denotes the degree of wave steepening attained by the system and it is inversely related to the shock thickness. Such resonant energy injection can be achieved via fluid dynamic instabilities or externally applied forcing. In thermoacoustic devices for example, the energy injection takes place due to thermoacoustic instabilities. The presence of nonlinear wave effects in thermoacoustics have been identified and studied experimentally [12,13] and numerically [4]. More recently, Gupta *et al.* [4] demonstrated the existence of an equilibrium

*sthirani@purdue.edu

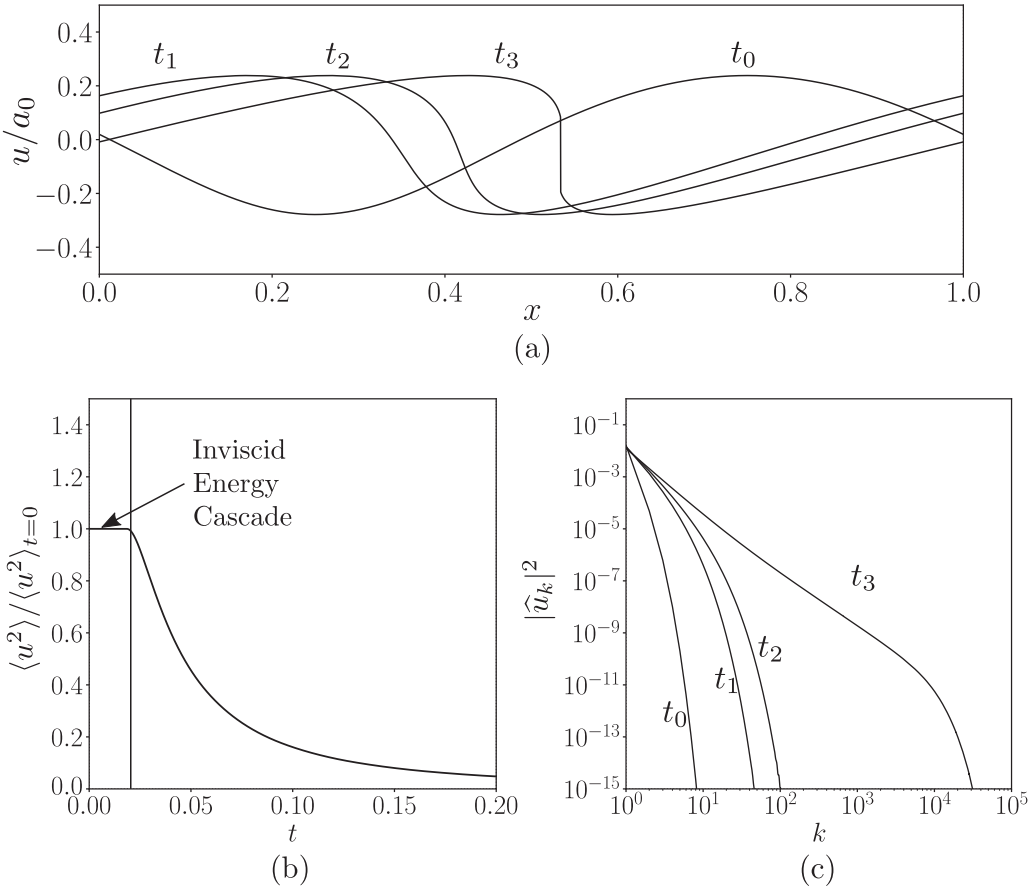

FIG. 1. Velocity perturbation in a high amplitude acoustic traveling wave (a), evolution of normalized spatial average of u^2 (b), and velocity spectra $|\hat{u}_k|^2$ (c) at times t_0, t_1, t_2, t_3. The spectral broadening occurs due to the nonlinear terms in the governing equations resulting in the energy cascade from larger to smaller length scales.

spectrum, resulting from a balance between the thermoacoustic energy production and thermoviscous dissipation at length scales corresponding to the shock thickness. Similar observations have been made experimentally for a gas in a resonance tube periodically driven by a piston oscillating at frequencies close to the fundamental frequency [2,14,15].

The aforementioned studies only focus on acoustic nonlinearities in dense gases, in most cases air at standard temperature and pressure (STP). However, nonlinear acoustic wave propagation also plays a crucial role in controlling transition to turbulence in high-speed boundary layers, which are often in rarefied flow conditions. In canonical cases, transition to turbulence is in fact governed by the amplification of ultrasonic waves with energy mostly confined in the boundary layer [16–19], acting as an acoustic wave guide. For such conditions, the flow can be considered in the rarefied regime merely due to the very high frequencies involved, and even more so for high-altitude flight with characteristic pressures and densities of the order of 1 kPa and 0.01kg/m^3, respectively. This consideration motivates the current work, in which we explore the effects of gas rarefaction on the behavior of resonant nonlinear acoustic waves.

Propagation of sound waves in rarefied media has been analyzed in great detail both experimentally [20–23] and numerically [24–27]. The Knudsen number, Kn, defined as the ratio of the molecular mean free path to the relevant physical length scale, quantifies the degree of rarefaction of a gas. For a single-frequency acoustic wave, the relevant length scale is taken as the acoustic wavelength. That is, even at standard atmospheric conditions, a high frequency wave, say 260 MHz [28], yields Knudsen numbers close to 0.02 and is, hence, in the rarefied regime. Based on this notion, experiments were conducted [20,21] focusing on noble gases only excited by a high frequency pulse (∼11 MHz) in a transmitter-receiver system to investigate acoustic wave propagation in a rarefied medium, with Knudsen numbers in the range 0.002–2. It was found that the attenuation rate of the sound wave increased with the Knudsen number, due to so-called *translational dispersion*: In rarefied environments, only the faster moving molecules contribute to the macroscopic wave transmission mechanism due to larger mean free path values, thus accelerating the high-frequency waves leading to wave dispersion and, hence, attenuation [28]. Inspired by these experimental attempts, we herein focus on a canonical flow setup; a one-dimensional system excited at its resonant frequency with Argon as the working fluid.

Other theoretical investigations [24–27] confirm the increase in the attenuation of the sound wave with increasing Knudsen number, also showing how Navier-Stokes-based solutions deviate from the experimental and kinetic theory results for high Knudsen numbers. This is not surprising, as the Navier-Stokes equations are based on a continuum

hypothesis and are hence not valid for high Knudsen numbers, where the Boltzmann equation is better suited. In this work, in fact, we have used the Navier-Stokes equations for cases with $\mathrm{Kn} < 0.01$ and the Boltzmann equation for $\mathrm{Kn} \geqslant 0.01$. The novelty of the present contribution lies in extending the degree of fidelity of the Navier-Stokes simulations to an advanced (weak-)shock-resolving numerical framework, as well as a systematic spanning of the Knudsen and acoustic Reynolds number space; the effects of the latter, in particular, have not been considered in previously. The approach adopted here in fact relies on the theoretical framework by Gupta and Scalo [11] on the nonlinear acoustic spectral energy cascade, which stresses the relative importance of nonlinear acoustic effects over thermoviscous dissipation, measured by the acoustic Reynolds number.

The paper is organized as follows. A description of the problem setup and the parameter space investigated is found in Sec. II. Details of the continuum gas dynamics equations and the associated numerical scheme are presented in Sec. III, followed in Sec. IV by a description of the Bhatnagar-Gross-Krook (BGK) model and the numerical scheme employed to solve it. The results from the simulations are presented in Sec. V, with subsections focused on comparison between the Navier-Stokes and BGK solutions, steepening of the planar acoustic wave and resonance amplitudes, fluctuation intensity profiles, the equilibrium spatial and temporal spectra, and the budgets for the base internal energy. We have also introduced scaling parameters to collapse the acoustic energy spectra in the wavenumber-frequency domain for different Knudsen numbers and provide an analytical estimate of the smallest length scale which is of the same order as shock-thickness.

II. PROBLEM SETUP

The problem setup, shown in Fig. 2, consists of a closed tube with a piston at one end, oscillating at the tube's fundamental resonant frequency ω_{res}, calculated as

$$\omega_{\mathrm{res}} = \pi a_0 / L, \tag{1}$$

and with instantaneous velocity,

$$u_p(t) = U_{p,\max} \sin(\omega_{\mathrm{res}} t), \tag{2}$$

where $U_{p,\max}$ is the piston velocity amplitude. The adiabatic speed of sound, a_0, is calculated at the initial base-state temperature of the gas. The walls of the tube and piston are considered adiabatic and the system is modeled only in one dimension, x, with total length, $L = 1$ m. The gas inside the tube is Argon.

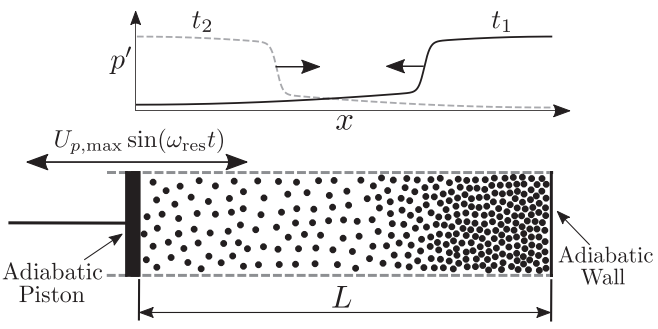

FIG. 2. Illustration of the investigated one-dimensional piston-tube setup during maximum compression of the gas at the adiabatic wall (t_1) and approximately 180° later in the shock resonance cycle (t_2).

We decompose the instantaneous pressure p, velocity u, density ρ, and temperature T, as

$$\begin{aligned} p &= p_0(\tau) + p'(x,t), \quad u = u_0 + u'(x,t), \\ \rho &= \rho_0 + \rho'(x,t), \quad T = T_0(\tau) + T'(x,t), \end{aligned} \tag{3}$$

where p', u', ρ', and T' are the corresponding fluctuating quantities. Here, x and t refer to the spatial and temporal coordinates respectively. The base state for velocity is zero, $u_0 = 0$. Since the domain is closed, the base density, ρ_0, is constant, and as discussed later, the base pressure, $p_0(\tau)$, and temperature, $T_0(\tau)$, increase following a slow timescale, τ, as

$$p_0(x,t) = p_0(t) \simeq p_0(\tau), \quad T_0(x,t) = T_0(t) \simeq T_0(\tau), \tag{4}$$

due to thermoviscous dissipation. All base-state quantities are spatially uniform.

As mentioned earlier, the Knudsen number is the ratio of the mean free path of the gas molecules to the characteristic (macroscopic) length scale of the problem; in the present context it can be written as the ratio of two timescales [29],

$$\mathrm{Kn} = \frac{1}{\sqrt{2\pi\gamma}} \frac{\omega_{\mathrm{res}}}{\nu} = \left(\frac{\mu}{p_0 L}\right) \sqrt{\frac{\pi K_B T_0}{2m}}, \tag{5}$$

where μ is the dynamic viscosity, ν is the collision frequency, $\gamma = 1.6702$ is the ratio of specific heats for Argon, $K_B = 1.38 \times 10^{-23}\ \mathrm{m^2 kg/s^2 K}$ is the Boltzmann constant and $m = 66.3 \times 10^{-27}$ kg is the molecular mass of Argon. Based on the piston velocity amplitude, we define the piston Reynolds number, Re_{u_p}, as,

$$\mathrm{Re}_{u_p} = \frac{\rho_0 U_{p,\max} L}{\mu}. \tag{6}$$

Later we define another (more dynamically relevant) Reynolds number based on the maximum velocity amplitude achieved in the domain, $U_{\max}$ [Eq. (26)].

We have spanned five orders of magnitude for Kn and three orders of magnitude for Re_{u_p} in our simulations (see Table I). As the Knudsen number approaches unity, the mean free path theoretically approaches the length of the domain, hence the base state inside the tube approaches near-vacuum conditions. To avoid such conditions, all the Kn values considered are below unity. The initial value for the base-state temperature of the gas is 300 K for all the cases and the base-state values for density and pressure are evaluated accordingly for each Knudsen number using Eq. (5). The initial base-state values used to achieve various Knudsen numbers are reported in Table II.

III. FULLY COMPRESSIBLE ONE-DIMENSIONAL NAVIER STOKES EQUATIONS

In this section, we present the fully compressible one-dimensional Navier Stokes equations in Sec. III A followed by a description of the numerical scheme used to solve them in Sec. III B.

TABLE I. Piston velocity amplitudes, $U_{p,\max}$, for the simulation parameter space considered.

$U_{p,\max}$	⟵ Dense $\mathrm{Kn} = 10^{-5}$	$\mathrm{Kn} = 10^{-4}$	$\mathrm{Kn} = 10^{-3}$	$\mathrm{Kn} = 10^{-2}$	Rarefied ⟶ $\mathrm{Kn} = 10^{-1}$
$\mathrm{Re}_{u_p} = 0.2$	4×10^{-4} m/s	4×10^{-3} m/s	0.04 m/s	0.4 m/s	4 m/s
$\mathrm{Re}_{u_p} = 0.02$	4×10^{-5} m/s	4×10^{-4} m/s	4×10^{-3} m/s	0.04 m/s	0.4 m/s
$\mathrm{Re}_{u_p} = 0.002$	4×10^{-6} m/s	4×10^{-5} m/s	4×10^{-4} m/s	4×10^{-3} m/s	0.04 m/s

A. Mathematical model

The fully compressible one-dimensional Navier Stokes equations comprise the conservation equations for mass, momentum, and energy for the system. They read

$$\frac{\partial \rho}{\partial t} + \frac{\partial (\rho u)}{\partial x} = 0, \tag{7}$$

$$\frac{\partial}{\partial t}(\rho u) + \frac{\partial}{\partial x}(\rho u^2) = -\frac{\partial p}{\partial x} + \frac{\partial}{\partial x}\left(\frac{4}{3}\mu \frac{\partial u}{\partial x}\right), \tag{8}$$

$$\frac{\partial}{\partial t}(\rho E) + \frac{\partial}{\partial x}[u(\rho E + p)] = \frac{\partial}{\partial x}\left[\frac{4}{3}u\left(\mu \frac{\partial u}{\partial x}\right)\right] - \frac{\partial q_x}{\partial x}, \tag{9}$$

where ρ, q_x, and E are the instantaneous density, heat flux in x direction, and total energy per unit mass, respectively. The total energy per unit mass, E, is defined as

$$E = C_v T + \tfrac{1}{2}u^2, \tag{10}$$

where C_v is the specific heat capacity at constant volume. Since only a monatomic gas (Argon) is considered in this work, bulk viscosity effects are neglected. The conservation equations are closed by the ideal gas equation of state,

$$p = \rho R T, \tag{11}$$

where T is the instantaneous temperature and $R = 208.132$ J/kg K is the specific gas constant. The dynamic viscosity is calculated using the power law, $\mu = \overline{\mu}(T/\overline{T})^r$, where $\overline{\mu}$, $\overline{T}$, and r are the reference dynamic viscosity, reference temperature, and the exponent for the power law, respectively. The values for $\overline{\mu}$, $\overline{T}$, and r are [30]

$$\overline{\mu} = 2.117 \times 10^{-5}\,\mathrm{Pa\,s}, \quad \overline{T} = 273.15\,\mathrm{K}, \; r = 0.81. \tag{12}$$

Please note that such reference values do not correspond to the ones used to define the initial base state in Table II.

B. Numerical scheme

We have performed shock-resolved direct numerical simulations (DNS), up to Mach number 1.01 of the compressible 1D Navier-Stokes Eqs. (7)–(9) and (11) with adaptive mesh refinement (AMR) [11] for cases up to $\mathrm{Kn} = 10^{-3}$. We have used the second-order Runge-Kutta scheme with a constant CFL of 0.5 for integrating the Navier-Stokes Eqs. (7)–(9) and (11) in time utilizing the staggered spectral difference (SD) spatial discretization approach introduced by Kopriva and Kolias [31]. In the SD approach, the domain is discretized into mesh elements and within each element, the Lagrange polynomial reconstruction of variables allows numerical differentiation with spectral accuracy.

To accurately resolve all length scales in the flow we have combined the SD approach with the AMR approach as first introduced by Mavriplis [32]. The AMR approach allows us to focus computational resources to adequately resolve unsteady shock waves. To this end, we expand the values of a generic variable ϕ local to the cell in the Legendre polynomial space as

$$\phi = \sum_{i=1}^{N} \tilde{\phi}_i \psi_i(x), \tag{13}$$

where $\psi_i(x)$ is the Legendre polynomial of $(i-1)$th degree. The polynomial coefficients, $\tilde{\phi}_i$, are utilized for estimating the local resolution error, ε, defined as [32]

$$\varepsilon = \left(\frac{2\tilde{\phi}_N^2}{2N+1} + \int_{N+1}^{\infty} \frac{2 f_\varepsilon^2(n)}{2n+1} dn\right)^{1/2}, \quad f_\varepsilon(n) = c e^{-\sigma n}, \tag{14}$$

where f_ε is the exponential fit through the coefficients of the last four modes in the Legendre polynomial space. As the estimated resolution error, ε, exceeds a predefined tolerance, the cell divides into two subcells, which are connected utilizing a binary tree. The subcells merge together if the resolution error decreases below a predefined limit. The numerical fluxes at cell interfaces were evaluated using the Harten-Lax-van Leer-contact (HLLC) Riemann solver [33]. A schematic of the spatial discretization scheme, the Lagrange polynomial reconstruction and the numerical flux interfaces, as used by Gupta and Scalo [11], is provided in Fig. 3.

TABLE II. Tabulation of initial base state values of density, pressure, and temperature for the span of Knudsen numbers considered, where $\rho_{\mathrm{ref}} = 1.1456 \times 10^{-2}\,\mathrm{kg/m^3}$, $p_{\mathrm{ref}} = 715.332\,\mathrm{Pa}$, and $T_{\mathrm{ref}} = 300$ K.

Initial base state values	⟵ Dense $\mathrm{Kn} = 10^{-5}$	$\mathrm{Kn} = 10^{-4}$	$\mathrm{Kn} = 10^{-3}$	$\mathrm{Kn} = 10^{-2}$	Rarefied ⟶ $\mathrm{Kn} = 10^{-1}$
p_0	p_{ref}	$10^{-1} p_{\mathrm{ref}}$	$10^{-2} p_{\mathrm{ref}}$	$10^{-3} p_{\mathrm{ref}}$	$10^{-4} p_{\mathrm{ref}}$
ρ_0	ρ_{ref}	$10^{-1} \rho_{\mathrm{ref}}$	$10^{-2} \rho_{\mathrm{ref}}$	$10^{-3} \rho_{\mathrm{ref}}$	$10^{-4} \rho_{\mathrm{ref}}$
T_0	T_{ref}	T_{ref}	T_{ref}	T_{ref}	T_{ref}

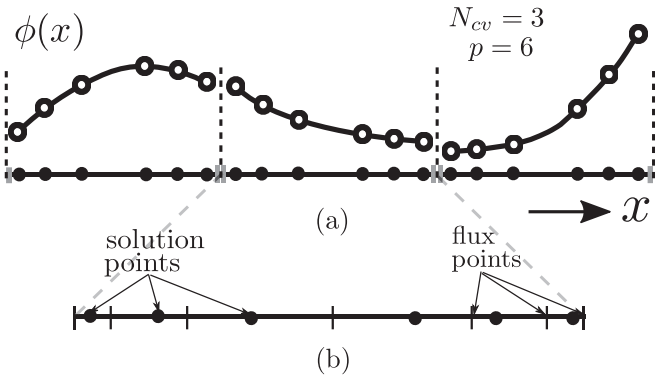

FIG. 3. Schematic of (a) the polynomial reconstruction of a quantity $\phi(x)$ over a one-dimensional domain consisting of three elements, and (b) the staggered spectral difference spatial discretization approach used with solution (•) and flux points (|) within a single element. N_{cv} is the number of elements and p is the number of solution points within an element.

IV. THE BOLTZMANN EQUATION

To study the effects of rarefaction on planar nonlinear acoustic waves for cases with Kn $= 10^{-1}$ and 10^{-2}, equations based on kinetic theory have been used. In the following, we introduce the Bhatnagar-Gross-Krook (BGK) equation, a model Boltzmann equation which is characterized by the use of a linearized model for the molecular collisions in Sec. IV A, and the numerical scheme used to solve it in Sec. IV B.

A. Mathematical model

The Boltzmann transport equation governs the evolution of the density distribution function, $f(\vec{x}, \vec{c}, t)$, where $\vec{c}$ refers to the molecular velocity space. In general, the density distribution function is a seven-dimensional quantity and depends on three dimensions in physical space, $\vec{x} = (x, y, z)$, three components of the molecular velocity space, $\vec{c} = (c_x, c_y, c_z)$, and time. The Boltzmann transport equation in such a case is given by

$$\frac{\partial f}{\partial t} + \vec{c} \cdot \nabla f = \mathcal{Q}, \tag{15}$$

where $\mathcal{Q}$ is the collision operator. The Boltzmann collision operator has the fundamental property of conserving mass, momentum and energy, that is

$$\int_{\vec{c}\in\mathbb{R}^3} \mathcal{Q}(f, f)\theta(\vec{c})d\vec{c} = 0, \quad \theta(\vec{c}) = 1, \vec{c}, |\vec{c}|^2. \tag{16}$$

For more details, the reader is referred to classic textbooks in molecular gas dynamics [30].

For simplicity, we consider the BGK model [34] for the Boltzmann transport equation restricted to one spatial dimension, given by

$$\frac{\partial f}{\partial t} + c_x \frac{\partial f}{\partial x} = \nu(f_\gamma - f), \tag{17}$$

where f_γ is the equilibrium distribution, given by the local Maxwellian distribution,

$$\mathcal{M}(\vec{c}) = \frac{\rho}{(2\pi RT)^{\frac{3}{2}}} \exp\left(-\frac{|\vec{c} - \vec{u}|^2}{2RT}\right), \tag{18}$$

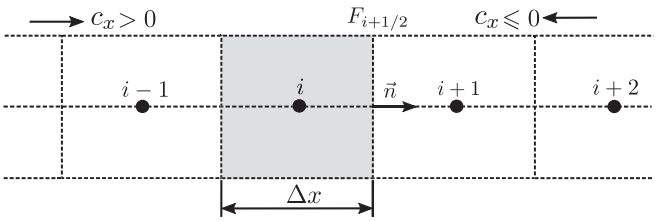

FIG. 4. Schematic of the staggered flux conservative spatial discretization used for the BGK solver depicting the flux faces (i+1/2) and cell centers (i).

where $\vec{u} = (u, v, w)$ is the macroscopic flow velocity. Other macroscopic parameters of the flow are calculated from moments of the density distribution function:

$$\rho = \int_{\vec{c}\in\mathbb{R}^3} f(\vec{c})d\vec{c}, \quad \rho\vec{u} = \int_{\vec{c}\in\mathbb{R}^3} \vec{c} f(\vec{c})d\vec{c},$$
$$T = \frac{1}{3\rho R} \int_{\vec{c}\in\mathbb{R}^3} |\vec{c} - \vec{u}|^2 f(\vec{c})d\vec{c}. \tag{19}$$

The pressure is then calculated by using the ideal gas equation of state. The collision frequency is calculated at each time step at every location in the physical space as

$$\nu = \frac{p}{\mu}, \tag{20}$$

where the dynamic viscosity, μ, for the gas is calculated using the power law described in Sec. III A.

The BGK model for the collision operator also conserves mass, momentum, and energy and preserves the Euler limit in the Chapman-Enskog expansion [29]. While the Prandtl number for Argon is 2/3, the BGK model equation naturally yields a Prandtl number of 1 in the Chapman-Enskog expansion. For the sake of consistency, the Navier-Stokes simulations have been run with unitary Prandtl number, despite being unphysical. Various numerical trials (not shown) reveal that varying the Prandtl number in the range from 2/3 to 1 in the Navier-Stokes simulations does not impact the conclusions of this manuscript nor yields significant quantitative changes in the results.

B. Numerical scheme

There are three broad categories of numerical schemes to solve the Boltzmann equation: discrete velocity method (DVM) [35–38], Fourier spectral methods [39–42], and direct simulation Monte Carlo (DSMC) [30,43–45]. We have utilized DVM [38] to solve the BGK equation, which involves discretization of the molecular velocity space. Consequently, the governing equations and associated integrals, such as Eqs. (17) and (19), are solved for in a discrete sense.

We have used the second-order Runge-Kutta scheme to integrate the BGK model equation in time, utilizing a staggered flux conservative approach for the spatial discretization. The flux points are collocated at the cell faces and the solution points at the cell centers as shown in Fig. 4. The second-order upwind QUICK [46] scheme has been used for the evaluation

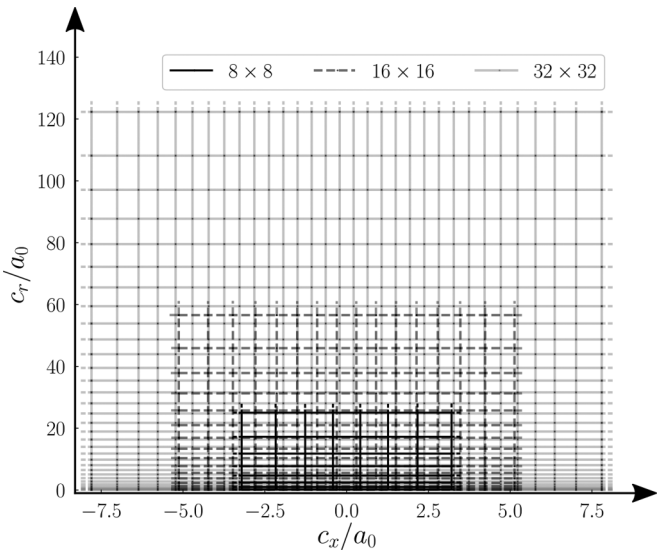

FIG. 5. Illustration of three grid sizes for the discretization of the molecular velocity space in c_x and c_r.

of fluxes at the flux faces and can be formulated as

$$\text{If } c_x|_{i+1/2} > 0 : F_{i+1/2} = \frac{c_x}{\Delta x}\left(\frac{6}{8}f_i + \frac{3}{8}f_{i+1} - \frac{1}{8}f_{i-1}\right),$$
$$\text{or } c_x|_{i+1/2} \leqslant 0 : F_{i+1/2} = \frac{c_x}{\Delta x}\left(\frac{6}{8}f_{i+1} + \frac{3}{8}f_i - \frac{1}{8}f_{i+2}\right). \tag{21}$$

Axial symmetry of the setup is used to reduce the molecular velocity components to two—axial and radial. For efficiency and speed of calculations, we have used Gauss-Hermite and Gauss-Laguerre polynomials to obtain the discretization points in the molecular velocity space in the axial and radial directions, respectively. Different grid sizes for integration in the molecular velocity space are shown in Fig. 5, where c_x and c_r refer to the molecular velocities in axial and radial directions, respectively. The domain for molecular velocity space used in this work is composed of 32×32 grid points.

The equilibrium distribution function was discretized as

$$\begin{aligned} f_\gamma &= \alpha_1 e^{\beta\cdot\mathbf{p}}, \\ \beta &= [-\alpha_2, \alpha_3, \alpha_4, \alpha_5], \\ \mathbf{p} &= \{[(c_x-u)^2 + (c_y-v)^2 + (c_z-w)^2, \ldots \\ &\quad \ldots(c_x-u), (c_y-v), (c_z-w)]\}^T, \end{aligned} \tag{22}$$

where the coefficients α_i are found by solving Eq. (16) using Newton's iteration method. The discrete form of the system of equations solved is shown in Eq. (23):

$$\sum_j f_\gamma \xi_j = \rho; \quad \sum_j c_x f_\gamma \xi_j = \rho u;$$
$$\sum_j c_y f_\gamma \xi_j = \rho v; \quad \sum_j c_z f_\gamma \xi_j = \rho w;$$
$$\sum_j \left(c_x^2 + c_y^2 + c_z^2\right) f_\gamma \xi_j = \rho(u^2+v^2+w^2) + \frac{3}{2}\rho T. \tag{23}$$

Here, ξ_j refers to the weights of the quadrature used for integration. This scheme was presented by Frezzotti [47] and has been evaluated computationally by Mieussens [48], Mieussens and Struchtrup [49], and Chigullapalli and Alexeenko [50].

Boundary conditions

As the problem considered here is one-dimensional in space, the only wall boundary conditions to be imposed are at the duct terminations, which we chose as adiabatic. This is implemented as specular boundary conditions [29] in the BGK solver, assuming total reflection with no diffusion effects from the wall and is modeled such that the values of f incident on the wall boundary are reflected back,

$$f[\vec{c}_j + (\vec{v}_{\text{wall}} \cdot \vec{n})\vec{n}] = f[\vec{c}_i - (\vec{v}_{\text{wall}} \cdot \vec{n})\vec{n}], \tag{24}$$

where the subscripts i and j represent the incident and reflected quantities and $\vec{v}_{\text{wall}}$ and $\vec{n}$ represent the velocity of the wall and wall normal, respectively.

V. RESULTS AND DISCUSSION

As the piston-tube setup (Fig. 2) is excited at the first resonant frequency of the system, the acoustic amplitude of the planar wave inside the tube increases until an equilibrium is reached between the large-scale energy injection into the system and the energy dissipation due to molecular collisions (viscosity). Figure 6 shows the time series of (a) pressure, p', and (b) velocity, u, fluctuations at $x = L$ and $x = L/2$, respectively, for the case of $\text{Re}_{u_p} = 0.2$ and $\text{Kn} = 10^{-5}$ (see Table I) as obtained from the Navier-Stokes solver with adaptive mesh refinement (NS-AMR). The insets (i) and (ii) show the different stages of wave steepening before a limit cycle, or equilibrium limit, is reached. The insets (i) highlight the harmonic regime in which the amplitude of the acoustic wave is small relative to the base pressure and the linearized governing equations are sufficient. The insets (ii) show the nonlinear regime during which energy begins to cascade from the fundamental resonant harmonic to higher harmonics in the frequency domain. In the physical space, this results in wave steepening. Continued injection of energy due to resonance results in saturation of the acoustic amplitude, characterized by a balance between the energy injected into the system and the thermoviscous dissipation—establishing an equilibrium energy cascade. Insets (iii) show this quasisteady regime, hereafter referred to as the limit cycle. The latter cannot be considered an equilibrium state for the overall system given the steady background heating caused by the thermoviscous dissipation (discussed later). Such slow-varying base-state quantities are obtained via sharp spectral temporal filtering of the numerical simulation data.

A. Comparison of Navier-Stokes and BGK solutions

In this section we present a comparison between the results from the Navier-Stokes and BGK equation solvers in a Knudsen number range typically considered of overlap between the two models. To this end, we show the temporal spectra of pressure and velocity at the limit cycle for the cases with $\text{Kn} = 10^{-1}$ and 10^{-2}. Since the signals are periodic at limit cycle, p' and u can be expressed as the following Fourier series

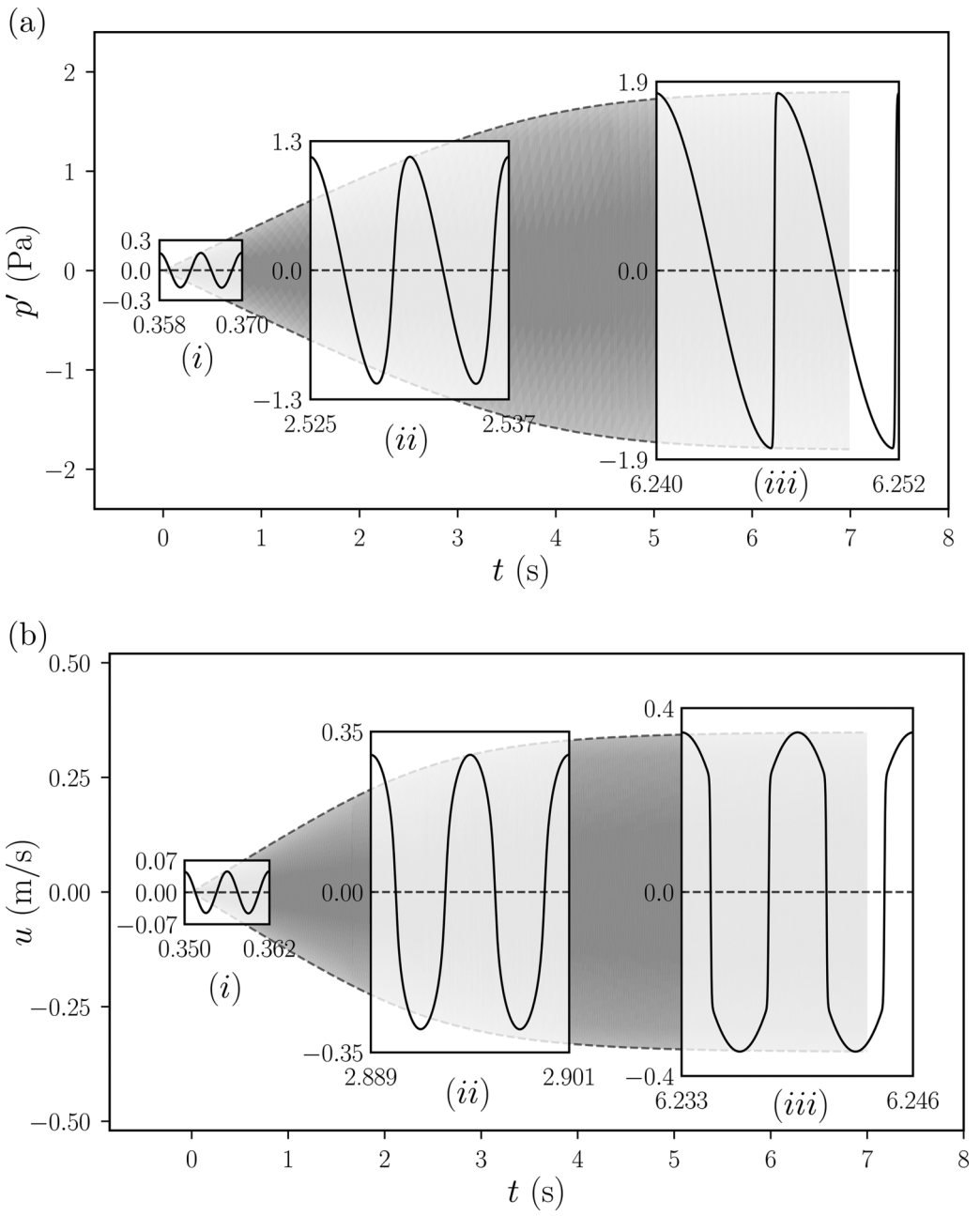

FIG. 6. Time series for (a) pressure fluctuations p' at $x = L$ and (b) velocity u at $x = L/2$ for $\mathrm{Re}_{u_p} = 0.2$ and $\mathrm{Kn} = 10^{-5}$ as obtained from the NS-AMR solver. The figure insets—(i), (ii) and (iii)—show the different stages in steepening of the planar acoustic wave until a limit cycle is achieved.

expansions:

$$u(t) = \sum_{\substack{k=-\infty \\ k\neq 0}}^{k=\infty} \widehat{u}(k) e^{i\omega_k t}, \quad p'(t) = \sum_{\substack{k=-\infty \\ k\neq 0}}^{k=\infty} \widehat{p}(k) e^{i\omega_k t}, \qquad (25)$$

where $\widehat{u}(k)$ and $\widehat{p}(k)$ are coefficients of the kth harmonic mode of the Fourier series expansion with frequency ω_k. The Fourier coefficients are extracted via a windowed Fourier transform over 20 acoustic periods based on time series at $x = L$ for p' and at $x = L/2$ for u (Fig. 6).

Figure 7 shows the comparison of the temporal spectra of p' and u as obtained from the NS-AMR solver with those from the BGK solver for $\mathrm{Kn} = 10^{-1}$ and $\mathrm{Kn} = 10^{-2}$ and varying Reynolds numbers Re_{u_p}. The pressure spectra are contiguous, while only odd numbered harmonics appear in the velocity spectra since the velocity signal is symmetric in time.

The difference in the solutions obtained from the two solvers decreases as the Reynolds number and Knudsen number decrease. Overall, the resonance response predicted by the NS-AMR solver (which should only be applied in the dense regime) is systematically lower than the one predicted from the BGK solver for $\mathrm{Kn} = 10^{-1}$ and $\mathrm{Kn} = 10^{-2}$.

Results from the NS-AMR solver seemingly under-predict acoustic energy levels for $\mathrm{Kn} \geqslant 10^{-2}$ with respect to the BGK counterpart, and are hence neglected for this range. On the

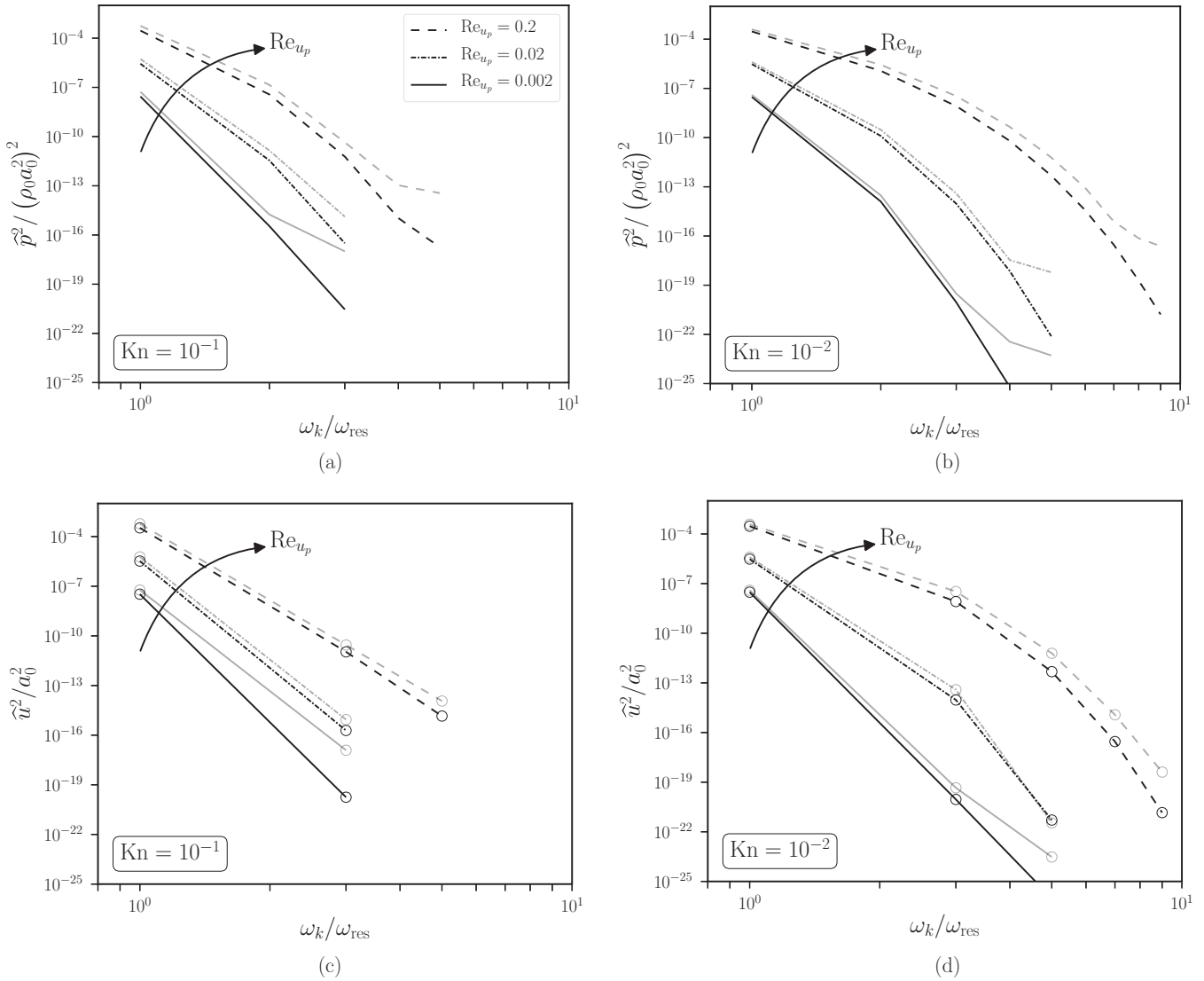

FIG. 7. Power spectral densities of pressure at $x = L$ (a, b) and velocity at $x = L/2$ (c, d) at the limit cycle for $\mathrm{Kn} = 10^{-1}$ and $\mathrm{Kn} = 10^{-2}$ from NS-AMR (black) and BGK (gray) solvers. Only the odd harmonics have been plotted for $\widehat{u}$. Spurious high-frequency or wavenumber content due to round-off errors has been omitted.

other hand, the use of the BGK solver will be restricted to cases with $\mathrm{Kn} \geqslant 10^{-2}$ (see Table III). Such choice also reduces the computational cost of spanning the full parameter space given in Table I with the BGK solver, which suffers from the stiff collision term for $\mathrm{Kn} < 10^{-2}$.

B. Wave steepening and resonant response

Figure 8 shows the instantaneous waveform shape as the Knudsen number of the system is varied, keeping Re_{u_p} constant. Figure 8(a) shows the spatial profile of normalized pressure perturbation ($p'/|p'|_{\max}$) at the limit cycle for $\mathrm{Re}_{u_p} = 0.2$ when the piston is at its mean position moving away from the cavity [$\omega_{\mathrm{res}} t = (2n+1)3\pi/2$ in Eq. (2)]. For Knudsen numbers $\mathrm{Kn} > 10^{-2}$ the pressure perturbation is qualitatively similar to a half cosine, with negligible to no nonlinear distortion. As the Knudsen number decreases (flow becomes denser), the limit cycle pressure perturbation profile steepens further and a resonating shock wave is observable in the tube. A similar observation can be made in Fig. 8(b), which shows the spatial profile of normalized velocity ($u/|u|_{\max}$) at

TABLE III. Tabulation of the list of cases solved for by each solver: Navier-Stokes equations with adaptive mesh refinement (NS-AMR), Boltzmann equation with BGK closure (BGK).

	⟵ Dense $\mathrm{Kn} = 10^{-5}$	$\mathrm{Kn} = 10^{-4}$	$\mathrm{Kn} = 10^{-3}$	$\mathrm{Kn} = 10^{-2}$	Rarefied ⟶ $\mathrm{Kn} = 10^{-1}$
$\mathrm{Re}_{u_p} = 0.2$	NS-AMR	NS-AMR	NS-AMR	BGK	BGK
$\mathrm{Re}_{u_p} = 0.02$	NS-AMR	NS-AMR	NS-AMR	BGK	BGK
$\mathrm{Re}_{u_p} = 0.002$	NS-AMR	NS-AMR	NS-AMR	BGK	BGK

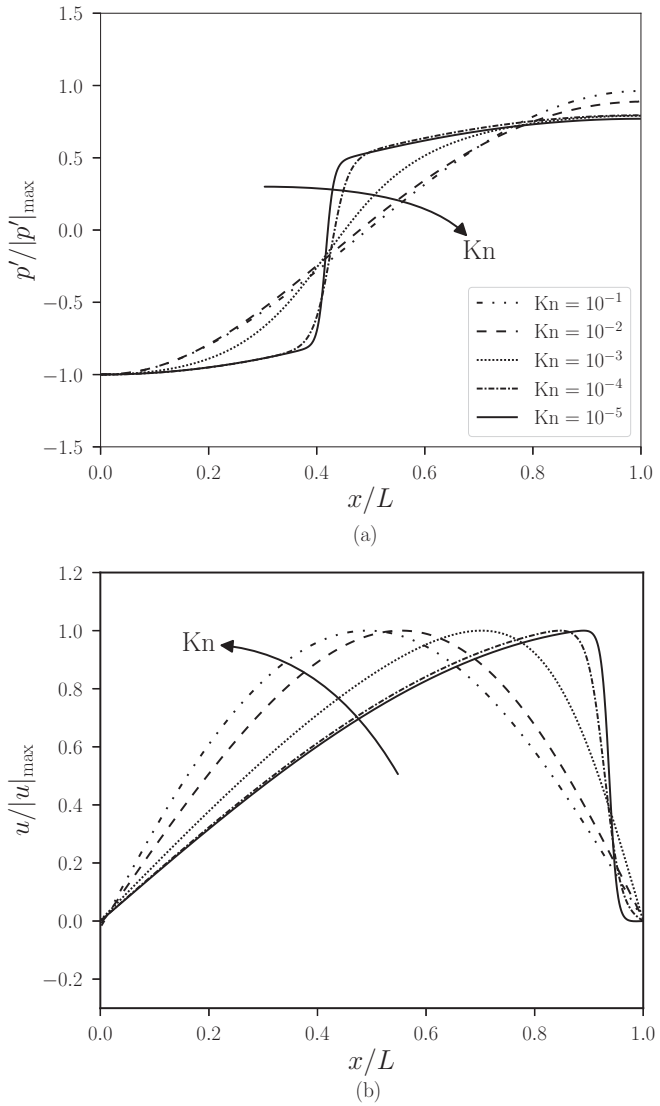

FIG. 8. Instantaneous profiles of (a) pressure fluctuation, p', and (b) velocity, u, normalized by their maximum values at the limit cycle for $\mathrm{Re}_{u_p} = 0.2$. The pressure field is plotted at the instance when the piston is at its mean position moving towards left, whereas the velocity is taken at the time instance when the piston is at its right extremum.

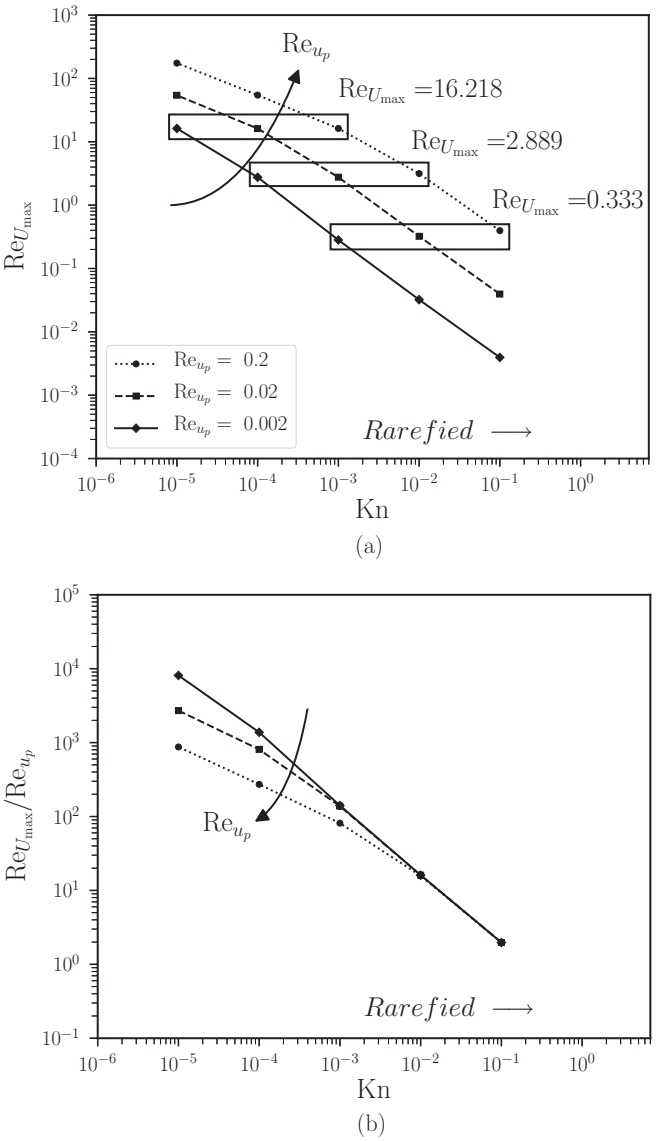

FIG. 9. Variation of $\mathrm{Re}_{U_{\max}}$ against Kn and Re_{u_p}: (a) depicts the behavior of $\mathrm{Re}_{U_{\max}}$ versus Knudsen number for all the cases considered and (b) illustrates $\mathrm{Re}_{U_{\max}}$ scaled by Re_{u_p} versus the Knudsen number. The degree of wave amplification due to resonance observed is the highest for the cases with the lowest Re_{u_p}.

the limit cycle for $\mathrm{Re}_{u_p} = 0.2$ when the piston is at its right extremum [$\omega_{\mathrm{res}} t = (2n+1)\pi$ in Eq. (2)]. The velocity profile for $\mathrm{Kn} = 10^{-1}$ is qualitatively similar (but not exactly equal) to a half sine, whereas for decreasing Knudsen numbers, the limit cycle velocity profile steepens and a shock wave is observed. Energy injection from the piston at the fundamental harmonic frequency sustains the shock wave at the limit cycle, which, for the specific piston-Reynolds number considered in this example, $\mathrm{Re}_{u_p} = 0.2$, is only present for $\mathrm{Kn} < 10^{-4}$.

To more appropriately quantify the limit cycle amplitude dependency on the Knudsen number of the gas (cf. Fig. 9), the following Reynolds number should be considered:

$$\mathrm{Re}_{U_{\max}} = \frac{\rho_0 U_{\max} L}{\mu}, \tag{26}$$

based on the maximum velocity amplitude in the domain, $U_{\max}$, occurring at approximately $x = L/2$ for all cases. $\mathrm{Re}_{U_{\max}}$ characterizes the relative importance of inertial to viscous forces more accurately than Re_{u_p}: the system can, in fact, achieve an increase of three orders of magnitude in $\mathrm{Re}_{U_{\max}}$ with a four-orders-of-magnitude decrease in the Knudsen number, for the same Re_{u_p} [Fig. 9(a)]. Consequently, the magnitude of maximum velocity amplitude in the tube for a fixed piston velocity amplitude also increases with decreasing Knudsen number, signifying a stronger resonant response of the system [cf. Fig. 9(b)]. The resonant energy injected into the system is balanced by thermoviscous dissipation, which increases with Knudsen number, resulting in an increase of the smallest length scale carrying acoustic energy, analogous to hydrodynamic turbulence [11]; in other words, as the wave steepening process establishes an energy cascade towards

higher wavenumbers, increasing the Knudsen number halts the cascade at larger length scales, thus preventing further amplification of the acoustic wave due to resonance and reducing the inertial range of inter-scale energy transfer (discussed later). In Fig. 9(a) three sets of cases, grouped by the same value of $\mathrm{Re}_{U_{\max}}$ (16.218, 2.889, and 0.333) for different values of Re_{u_p} and Kn are highlighted and will be used, hereafter, when needed, to rigorously isolate Knudsen number effects from Reynolds number effects, the latter being $\mathrm{Re}_{U_{\max}}$ and not Re_{u_p}.

C. Fluctuation intensity profiles

Besides affecting the resonant response, which is quantified by the ratio of the maximum velocity fluctuation amplitude in the domain to the piston velocity amplitude [Fig. 9(b)], the Knudsen number also affects the spatial pattern of fluctuation intensities at the limit cycle. Figure 10 shows the spatial profiles of intensity of pressure and velocity fluctuations, defined respectively as

$$p'_{\mathrm{rms}}(x) = \sqrt{\frac{1}{N}\sum_{n=0}^{N-1} p'(x,t_n)^2},$$
$$u_{\mathrm{rms}}(x) = \sqrt{\frac{1}{N}\sum_{n=0}^{N-1} u(x,t_n)^2}, \tag{27}$$

for $\mathrm{Re}_{u_p} = 0.02$, and where N is the number of samples in time over an acoustic period at the limit cycle. Using the Fourier coefficients and Parseval's identity, the sum of squares of point-wise pressure and velocity fluctuation values in the above equation can be evaluated as

$$\sum_{n=0}^{N-1} p'(t_n)^2 = 2\pi \sum_{k=0}^{N-1} |\widehat{p}(k)|^2,$$
$$\sum_{n=0}^{N-1} u(t_n)^2 = 2\pi \sum_{k=0}^{N-1} |\widehat{u}(k)|^2. \tag{28}$$

With increasing Knudsen number, the spatial profile of pressure fluctuation amplitude displays a progressively more defined pressure node at the center for increasing Kn, which is associated to a decrease in acoustic power emanating from the piston and being transmitted through the tube. For very low Knudsen numbers, the intensity profile remains relatively flat due to the redistribution of pressure fluctuation intensity by the resonating shock wave. With increasing Knudsen number, the deviation of the velocity fluctuation intensity profile from the fluctuation intensity at the piston decreases indicating less fluctuation amplification and hence a weaker resonant response.

In the following, we study the distribution of temporal Fourier coefficients with varying Knudsen number, to quantify the degree of nonlinear wave steepening and the consequent higher harmonic generation.

D. Spectral analysis and scaling of spectral quantities

Figure 11 shows the variation of distribution of temporal Fourier coefficients of pressure and velocity fluctuations, $\widehat{p}^2$ (taken at $x = L$) and $\widehat{u}^2$ (taken at $x = L/2$), respectively, at the limit cycle for varying Knudsen numbers for $\mathrm{Re}_{u_p} = 0.2$. We note that the range of frequencies spanned by both sets of spectra increases with decreasing Knudsen number displaying a -2 slope over more than a decade on a log-log scale at the limit cycle. A similar behavior is observed in hydrodynamic turbulence, where such range of scales is associated with inviscid spectral energy cascade in equilibrium conditions. Hereafter, this range of scales will be referred to as the *inertial range*. However, in nonlinear acoustics, such power law range of spectra exhibits thermoviscous dissipation as well, unlike hydrodynamic turbulence, as shown by Gupta and Scalo [11]. The highest energy-containing frequency in the spectra is associated with the smallest length scale in the flow, which corresponds to the thickness of the shock (when present). As discussed previously, with increasing Knudsen number the dissipation increases resulting in a decrease in the

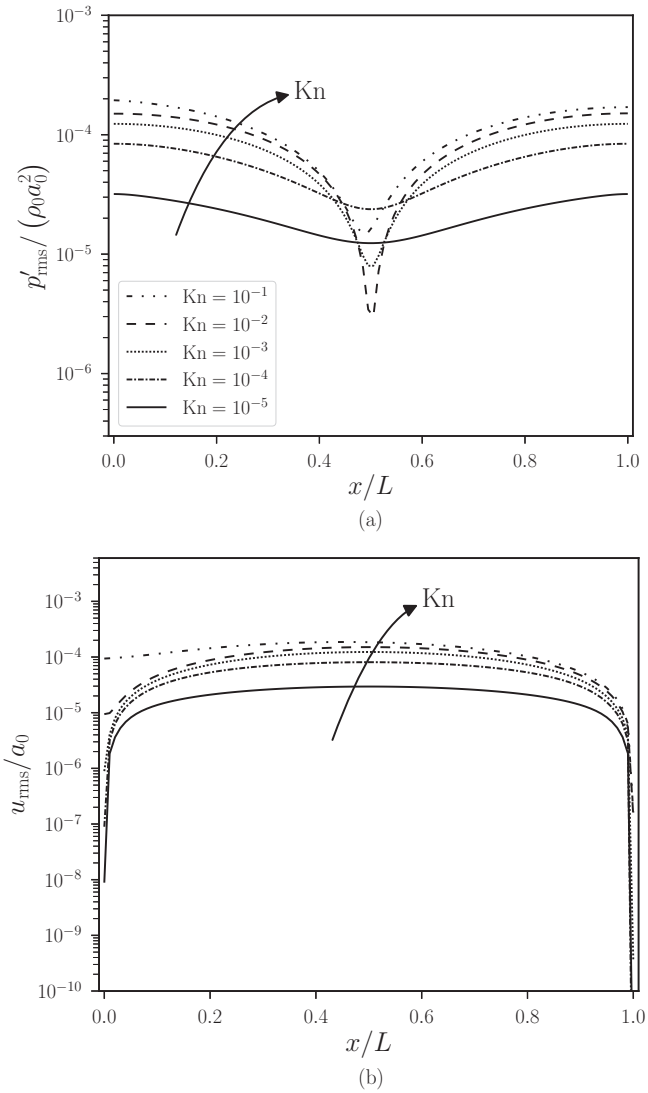

FIG. 10. Spatial variation of (a) pressure fluctuation intensity, p'_{rms}, and (b) velocity fluctuation intensity, u_{rms}, at the limit cycle versus x for $\mathrm{Re}_{u_p} = 0.02$. For increasing Knudsen number, the p'_{rms} profile becomes sharper at the center indicating decreased movement of the pressure node at the center.

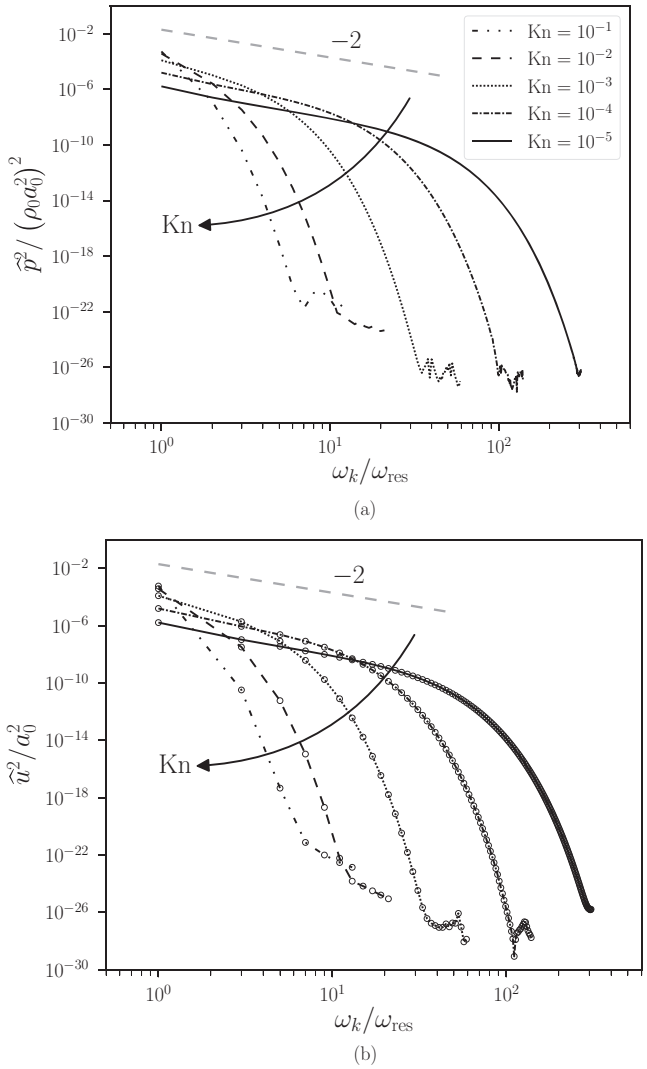

FIG. 11. Comparison of the temporal spectra at the limit cycle for $\text{Re}_{u_p} = 0.2$ (a) for pressure at $x = L$ and (b) velocity at $x = L/2$, for which only the odd harmonics are shown. Spurious high-frequency or wavenumber content due to round-off errors has been omitted.

highest acoustic frequency generated, shortening the inertial range; this is linked to an effective reduction of the $\text{Re}_{U_{\max}}$. Consequently, as shown in Fig. 8 the waveform at limit cycle exhibits energy only in larger length scales (it is less steepened) for higher Knudsen numbers, if Re_{u_p} is kept constant.

As shown by Gupta and Scalo [11], the smallest length scale generated due to nonlinear wave steepening can be estimated by closing the spectral energy budgets of wave perturbation. The perturbation energy for second-order nonlinear acoustic waves yielding the Lyapunov function of the system is given by [11,51]

$$E(p', u) = \frac{u^2}{2a_0^2} + \frac{p'^2}{2\left(\rho_0 a_0^2\right)^2} + f(p'), \tag{29}$$

where the energy correction term $f(p')$ is given by

$$f(p') = -\frac{2\gamma}{(\gamma-1)(2\gamma-1)} \times \left[\left(1+\frac{\gamma p'}{\rho_0 a_0^2}\right)^{1/\gamma} - 1 - \frac{p'}{\rho_0 a_0^2} + \frac{(\gamma-1)p'^2}{2\left(\rho_0 a_0^2\right)^2}\right]. \tag{30}$$

Utilizing the second-order perturbation energy [Eq. (29)] we define a characteristic dimensionless perturbation amplitude, A_{rms}, as

$$A_{\text{rms}} = \sqrt{\langle E \rangle}, \tag{31}$$

where $\langle . \rangle$ is the spatial averaging operator,

$$\langle . \rangle = \frac{1}{L}\int_0^L (.)dx. \tag{32}$$

Since the generation and dissipation of energy are balanced at the limit cycle, the cycle-averaged value of the perturbation energy [Eq. (29)] reaches a maximum in time. Balancing the characteristic rate of energy transfer from large scales to small scales, with the rate of viscous energy dissipation, yields the following order-of-magnitude equivalence [11]:

$$\frac{A_{\text{rms}}^2}{\eta} \sim \delta \frac{A_{\text{rms}}}{\eta^2}, \tag{33}$$

where $\eta \sim \delta/A_{\text{rms}}$ is the acoustic Kolmogorov length scale, i.e., the shortest length scale, analogous to the Kolmogorov length scale in turbulence, carrying acoustic energy; δ is the thermoviscous diffusivity defined as

$$\delta = \frac{\mu}{\rho_0 a_0 L}\left(\frac{4}{3} + \frac{\gamma-1}{\text{Pr}}\right), \tag{34}$$

where Pr is the Prandtl number. Analogously to the shortest length scale, the smallest timescale, τ_η, can be evaluated as

$$\tau_\eta = \frac{\eta}{a_0}. \tag{35}$$

Utilizing Eq. (29), the spectral energy $\widehat{E}_k$ can be defined as [11]

$$\widehat{E}_k = \frac{|\widehat{u}(k)|^2}{2a_0^2} + \frac{|\widehat{p}(k)|^2}{2\left(\rho_0 a_0^2\right)^2} + \Re\left[\widehat{p}(-k)\left(\widehat{\frac{f(p')}{p'}}\right)_k\right]. \tag{36}$$

Figure 12 (top row) shows the distribution of spectral energy $\widehat{E}_k$ with the frequencies scaled by the fundamental frequency of the system. In each subfigure we compare cases with same $\text{Re}_{U_{\max}}$, which actually quantifies the limit cycle energy in the system. Figure 12 (bottom row) shows the scaled spectral energy $\widehat{E}_k A_{\text{rms}}^{-2}$ versus frequency scaled with the smallest timescale τ_η for the three sets of cases grouped by $\text{Re}_{U_{\max}}$. We note that scaling the frequency with smallest timescale τ_η reveals an almost exclusively sub-Kolmogorov acoustic energy range for $\text{Re}_{U_{\max}} < 10$. This provides a quantitative estimate of when to expect the formation of an inertial range i.e., $\text{Re}_{U_{\max}} > 100$, as achieved in the cases with lower Kn in Fig. 11, characterized by the universal -2 slope of the inertial range. The latter is never actually observable in the cases shown in Fig. 12.

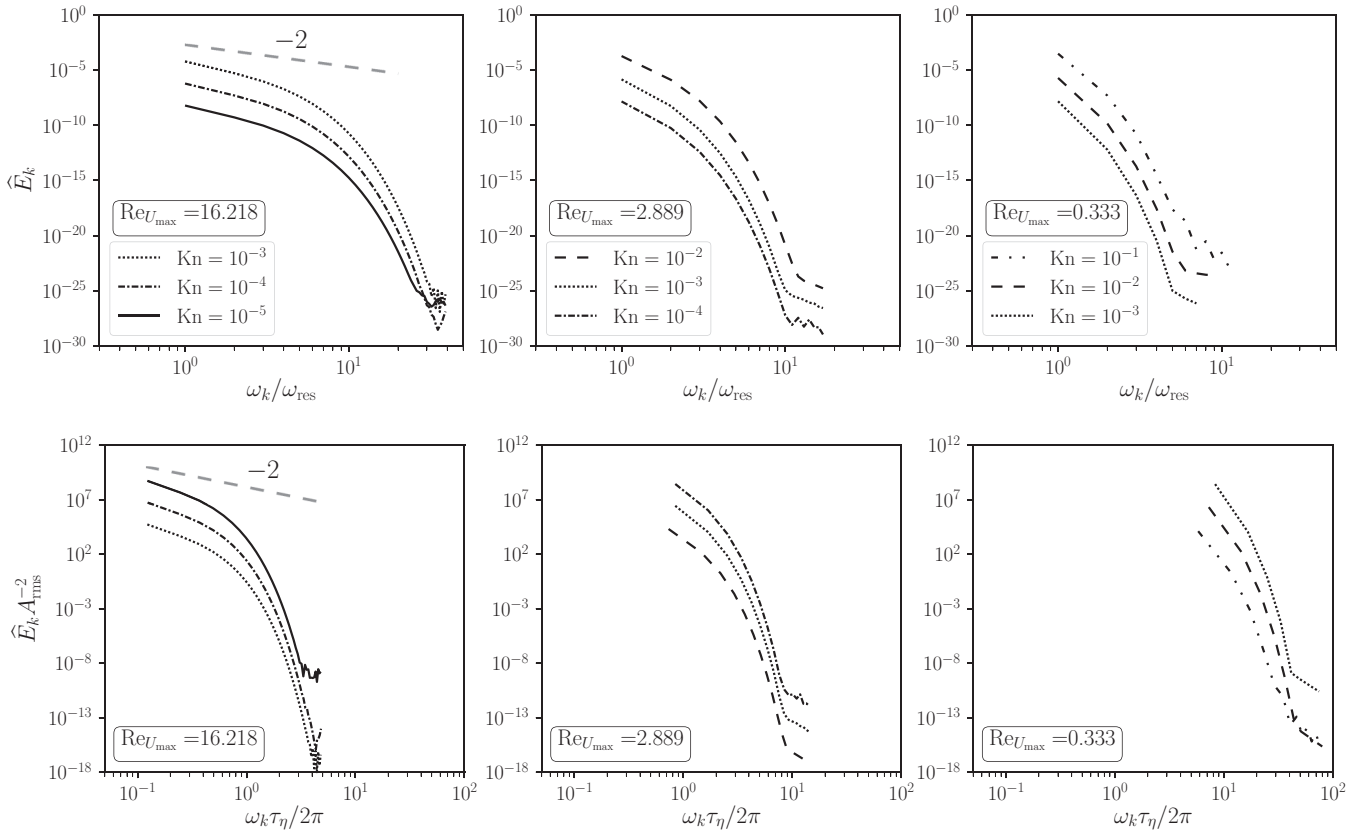

FIG. 12. Comparison of the temporal spectra of $\widehat{E}_k$ at the limit cycle for $\mathrm{Re}_{U_{max}} = 16.218$ (left); 2.889 (mid); 0.333 (right) at $x = L/2$. Spurious high-frequency or wavenumber content due to round-off errors has been omitted.

The spectra are collapsed along the frequency axis via the normalization $\omega_k\tau_\eta$, but not in amplitude by A_{rms}. This indicates that the (dimensionless) bandwidth of the spectral energy cascade increases with $\mathrm{Re}_{U_{max}}$.

To perform a wavenumber analysis of the spatial profiles of p' and u, a complex Fourier series expansion can not be used. Due to the computational setup considered, cosine and sine series expansions are used for the pressure and velocity, respectively. The corresponding spatial Fourier coefficients, $\widehat{P}$ and $\widehat{U}$, of p' and u, respectively, can then be evaluated as

$$\widehat{P}(k) = \sum_{n=0}^{N-1} p'(x_n)\cos\left[\frac{\pi}{N}\left(n+\frac{1}{2}\right)k\right], \quad k = 0, ..., N-1, \tag{37}$$

$$\widehat{U}(k) = \sum_{n=0}^{N-1} p'(x_n)\sin\left[\frac{\pi}{N}\left(n+\frac{1}{2}\right)(k+1)\right], \quad k = 0, ..., N-1, \tag{38}$$

where N is equal to the number of points in the spatial grid. Figures 13(a) and 13(b) show the variation of distribution of cycle-averaged spatial Fourier coefficients of pressure and velocity fluctuations, $\widehat{P}^2$ and $\widehat{U}^2$, respectively, at the limit cycle for varying Knudsen numbers for $\mathrm{Re}_{u_p} = 0.2$. Similar to the trend observed for temporal spectra (Fig. 11), the range of wavenumbers spanned by both sets of spectra increases with decreasing Knudsen number indicating an increase in the steepness of the waveform as shown in Fig. 8. The range of wavenumbers spanned by both sets of spectra increases with decreasing Knudsen number displaying a -2 slope over more than a decade on a log-log scale at the limit cycle.

Utilizing Eq. (29), the spectral energy in wavenumber space, $\widehat{E}_{sp,k}$, can be written as [11]

$$\widehat{E}_{sp,k} = \frac{|\widehat{U}(k)|^2}{2a_0^2} + \frac{|\widehat{P}(k)|^2}{2\left(\rho_0 a_0^2\right)^2} + \Re\left[\widehat{P}(-k)\left(\widehat{\frac{f(p')}{p'}}\right)_k\right]. \tag{39}$$

Figure 14(a) shows the distribution of cycle-averaged $\widehat{E}_{sp,k}$ with the wavenumber scaled by the length of the tube, for the three sets of cases with same $\mathrm{Re}_{U_{max}}$ at the limit cycle. Figure 14(b) shows the distribution of cycle-averaged scaled spectral energy, $\widehat{E}_{sp,k}A_{rms}^{-2}$, versus scaled wavenumber, $k\eta$, for the three sets of cases with same $\mathrm{Re}_{U_{max}}$ at the limit cycle. As observed in the temporal spectra (Fig. 12), the highest scaled wavenumber, $k\eta$, is much larger than unity, confirming that the acoustic activity is in the sub-Kolmogorov range in space and that $\mathrm{Re}_{U_{max}} = 16$ is not high enough to yield a proper inertial range (with -2 slope).

To quantify the rate of spectral energy cascade, we define the spectral energy flux, $\widehat{\Pi}_k$, from wavenumbers $|k'| \leqslant k$ to

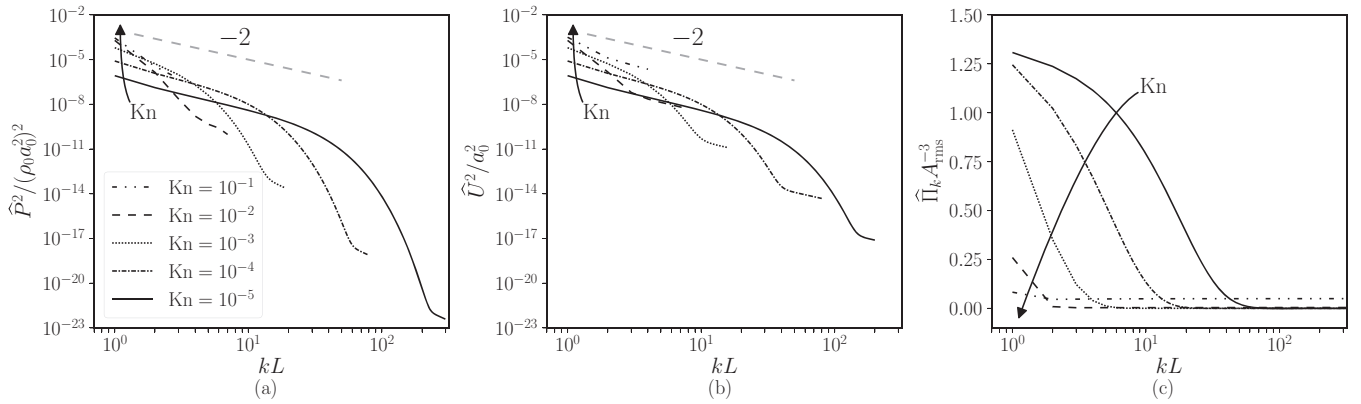

FIG. 13. Comparison of the cycle-averaged spatial spectra of (a) $p'(x)$ and (b) $u(x)$, and cycle-averaged (c) spectral flux, $\widehat{\Pi}_k$, scaled by A_{rms}, at the limit cycle for $\mathrm{Re}_{u_p} = 0.2$. Spurious high-frequency or wavenumber content due to round-off errors has been omitted. The $\mathrm{Re}_{U_{\max}}$ values for $\mathrm{Kn} = 10^{-1},\ 10^{-2},\ 10^{-3},\ 10^{-4}$, and 10^{-5} are 0.396, 3.153, 16.252, 54.518, and 174.571, respectively, at the limit cycle for $\mathrm{Re}_{u_p} = 0.2$.

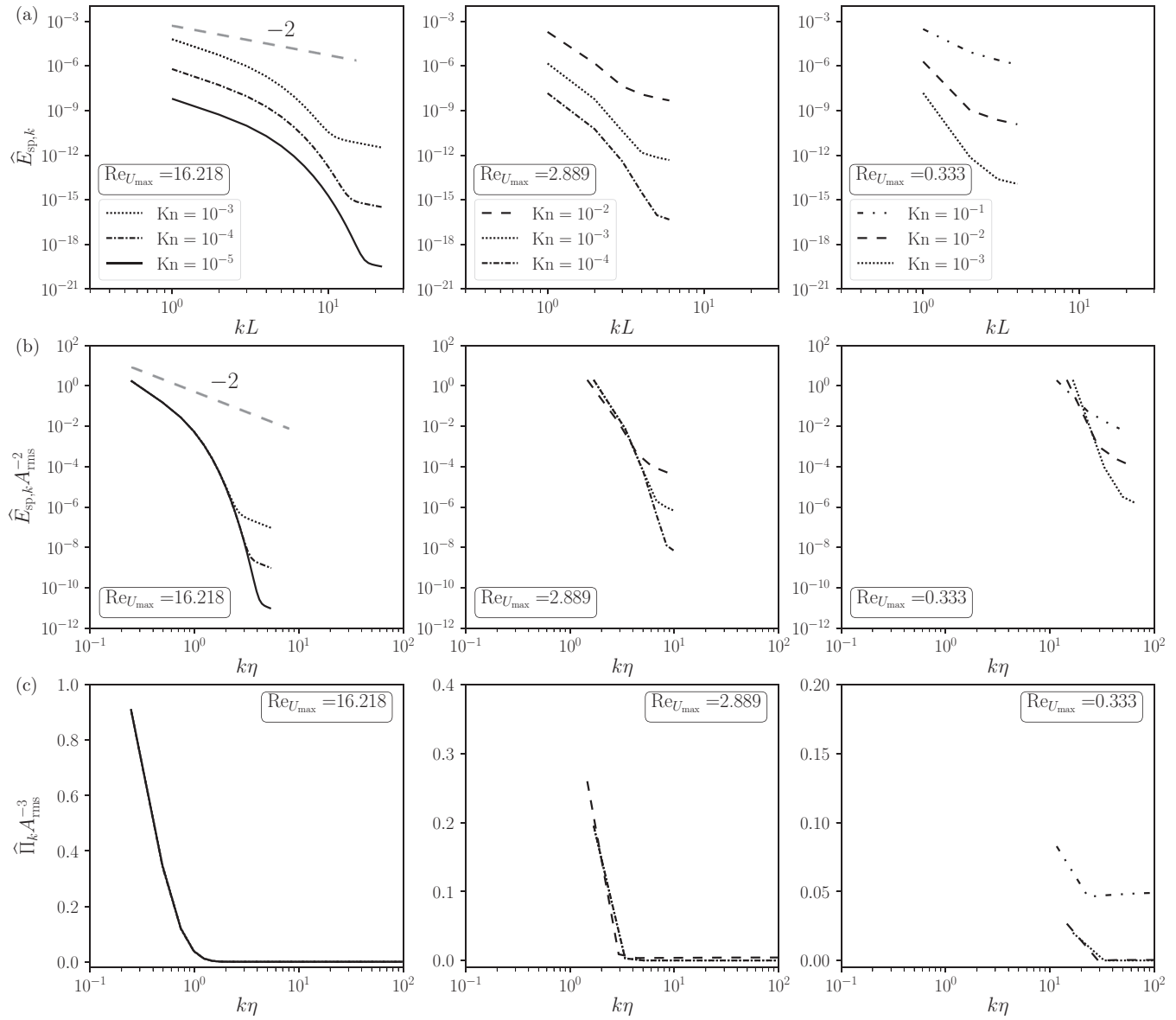

FIG. 14. Comparison of the cycle-averaged spatial spectra of (a, b) $\widehat{E}_{\mathrm{sp},k}$ and cycle-averaged (c) spectral flux, $\widehat{\Pi}_k$, at the limit cycle for $\mathrm{Re}_{U_{\max}} = 16.218$ (left); 2.889 (mid); 0.333 (right). Spurious high-frequency or wavenumber content due to round-off errors has been omitted.

$|k'| > k$ as [11]

$$\widehat{\Pi}_k = \sum_{|k'|\leqslant k} \Re\left[\frac{\widehat{P}_{-k'}}{\rho_0 a_0^2}\left(\frac{1}{a_0}\frac{\partial(\widehat{u'g})}{\partial x}\right)_{k'} + \frac{\widehat{P}_{-k'}}{\rho_0 a_0^2}\left(\frac{\widehat{u'}}{\rho_0 a_0^3}\frac{\partial p'}{\partial x}\right)_{k'} + \frac{1}{2}\frac{\widehat{U}_{-k'}}{a_0}\frac{\partial}{\partial x}\left(\frac{u'^2}{a_0^2} - \frac{p'^2}{(\rho_0 a_0^2)^2}\right)_{k'}\right], \tag{40}$$

where the function g is defined as [11]

$$g(p') = \frac{\gamma}{\gamma - 1}\left[\left(1 + \frac{\gamma p'}{\rho_0 a_0^2}\right)^{1/\gamma} - 1 - \frac{p'}{\rho_0 a_0^2}\right]. \tag{41}$$

Figure 13(c) shows the distribution of cycle-averaged spectral energy flux, $\widehat{\Pi}_k$, scaled by A_{rms}^{-3}, versus the wavenumber scaled by the length of the tube, at limit cycle for cases with $\text{Re}_{u_p} = 0.2$. Figure 14(c) shows the distribution of cycle-averaged spectral energy flux, $\widehat{\Pi}_k$, scaled by A_{rms}^{-3}, versus scaled wavenumber, $k\eta$, for the three sets of cases with same $\text{Re}_{U_{\max}}$ at the limit cycle. The high negative gradient of the distribution implies that all of the acoustic energy in the system is exhibited within the dissipation range of the spectra, and the absence of an inertial range for these sets of cases. The trend observed for the maximum value of $\widehat{\Pi}_k A_{\text{rms}}^{-3}$ at lower wavenumbers further confirms that a proper inertial range (with -2 slope) will be observed only for $\text{Re}_{U_{\max}} > 100$ [see Fig. 13(c)].

The acoustic energy dissipated by thermoviscous dissipation is converted into base internal energy and leads to an increase in the base-state pressure and temperature as mentioned before in Sec. II. In the subsection below, we quantify the Knudsen number effects on this process.

E. Base heating rates and thermal energy budgets

The base pressure, p_0, and temperature, T_0, of the system increase slowly in time due to the conversion of acoustic energy to heat by thermoviscous dissipation. To quantify the Knudsen number dependence of such heating, we evaluate the rate of change in internal energy with the slow timescale, τ, introduced in Sec. II. The governing equation for spatio-temporal evolution of internal energy for a compressible fluid in one dimension can be derived from Eqs. (8) and (9) as

$$\frac{\partial(\rho e)}{\partial t} + \frac{\partial(\rho u e)}{\partial x} = \frac{\mu C_p}{\text{Pr}}\frac{\partial^2 T}{\partial x^2} + \frac{4}{3}\mu\left(\frac{\partial u}{\partial x}\right)^2 - p\frac{\partial u}{\partial x}, \tag{42}$$

where e is the internal energy and C_p is the specific heat capacity at constant pressure. Using $C_v = R/(\gamma - 1)$ and the ideal gas equation of state, Eq. (42) can be modified to

$$\frac{\partial p}{\partial t} + \frac{\partial(pu)}{\partial x} = (\gamma - 1)\frac{\partial}{\partial x}\left(\frac{\mu C_p}{\text{Pr}}\frac{\partial T}{\partial x}\right) + (\gamma - 1)\frac{4}{3}\mu\left(\frac{\partial u}{\partial x}\right)^2 + (1 - \gamma)\frac{\partial pu}{\partial x} + (\gamma - 1)u\frac{\partial p}{\partial x}. \tag{43}$$

Equation (43) governs the rate of change of pressure in time due to thermal conduction, viscous dissipation, and acoustic nonlinearities. As mentioned before [see Eq. (3)], p, T and u can be decomposed into rapidly fluctuating acoustic quantities and slowly evolving base quantities. To obtain an equation for the slowly increasing base pressure, $p_0(\tau)$, we apply a sharp spectral filter in time to Eq. (43). For a generic variable φ, the sharp spectral filter is defined as

$$\overline{\varphi} = \mathcal{F}(\varphi; \omega_{\text{cut}}), \quad \omega_{\text{cut}} < \omega_{\text{res}}, \tag{44}$$

where $\mathcal{F}$ is the sharp spectral filter operator with cutoff frequency ω_{cut} and φ can be decomposed into its mean and perturbed values as $\varphi = \overline{\varphi} + \varphi'$. Moreover, by definition $\mathcal{F}(\varphi', \omega_{\text{cut}}) = \overline{\varphi'} = 0$.

Substituting the decomposition [Eq. (3)] for p, u, and T, and applying the sharp spectral filter to Eq. (43), we get

$$\frac{\partial p_0}{\partial \tau} + \gamma\frac{\partial\overline{(p'u')}}{\partial x} = (\gamma - 1)\frac{4}{3}\mu\overline{\left(\frac{\partial u'}{\partial x}\right)^2} + (\gamma - 1)\overline{u'\frac{\partial p'}{\partial x}}. \tag{45}$$

The thermal conduction term in Eq. (43) drops out upon filtering since all base-state quantities are considered spatially uniform (see Sec. II). Defining the mean acoustic power, $\dot{W}_{\text{ac}}$, dissipation rate, Φ, and mean mechanical work, Γ, as

$$\dot{W}_{\text{ac}} = \overline{(p'u')}, \quad \Phi = \frac{4}{3}\mu\overline{\left(\frac{\partial u'}{\partial x}\right)^2}, \quad \Gamma = \overline{u'\frac{\partial p'}{\partial x}}, \tag{46}$$

Eq. (45) can be compactly written as

$$\frac{\partial p_0}{\partial \tau} + \gamma\frac{\partial}{\partial x}\dot{W}_{\text{ac}} = (\gamma - 1)\Phi + (\gamma - 1)\Gamma. \tag{47}$$

Equation (47) yields the rate of change of base pressure, p_0, with the slow time, τ, in terms of cycle-averaged acoustic power, viscous dissipation rate, and the cycle-averaged mechanical work. Figure 15 shows the spatial variation of the mean acoustic power, $\dot{W}_{\text{ac}}$, or acoustic energy flux. The negative gradient of acoustic energy flux, see Fig. 16(a), is due to the energy injection by the piston at the left end of the tube. The acoustic energy flux is higher away from the piston for denser regimes indicating that the acoustic energy is

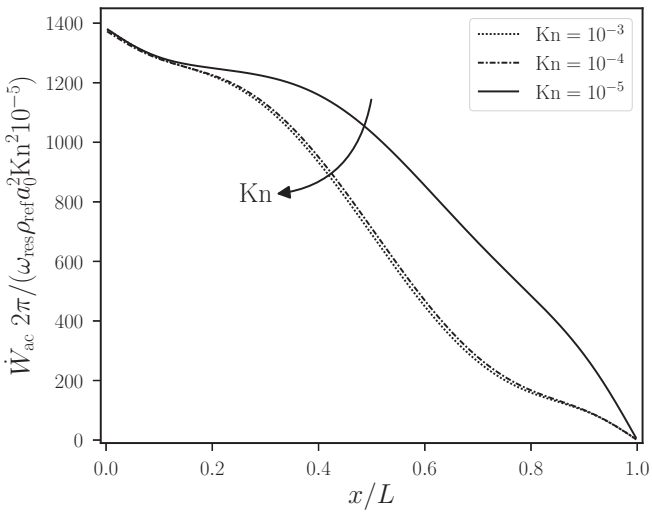

FIG. 15. Spatial variation of scaled mean acoustic power $\dot{W}_{\text{ac}}$ for the cases with $\text{Re}_{U_{\max}} = 16.218$. The decreasing trend of the acoustic power with x indicates that the acoustic power is directed towards the right of Fig. 2 with influx of acoustic energy at the left end from the piston.

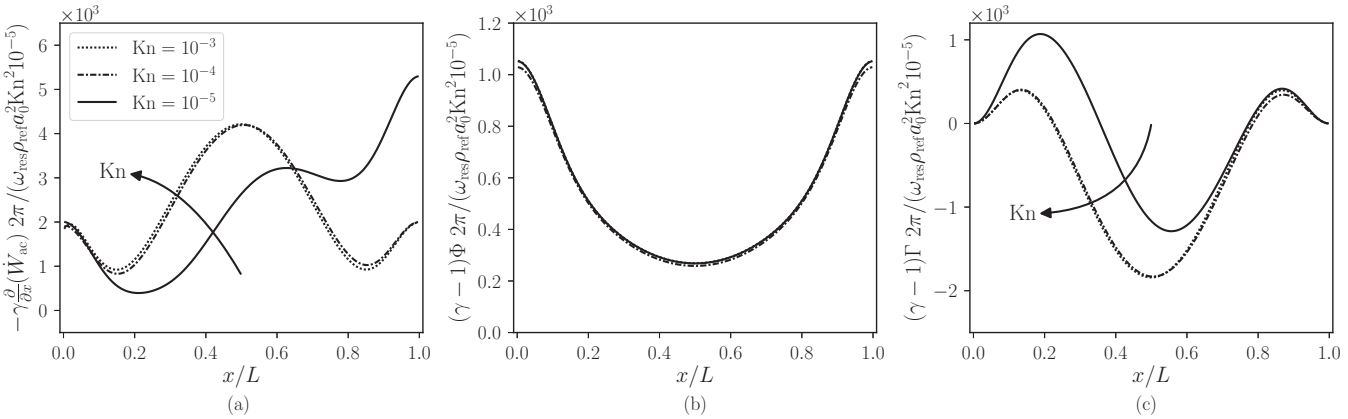

FIG. 16. Spatial variation of (a) scaled mean acoustic power derivative $\partial \dot{W}_{ac}/\partial x$, (b) dissipation Φ, and (c) acoustic mechanical work Γ versus x for the set of cases with $\mathrm{Re}_{U_{max}} = 16.218$.

transferred farther in denser gases, i.e., the acoustic near-field extends further in denser media. Figures 16(b) and 16(c) show the scaled dissipation and acoustic mechanical work terms in Eq. (47). Since the velocity gradients are maximum at the hard end walls, the viscous dissipation term, Φ, is maximum at the ends of the tube and increases with the Knudsen number as Kn^2. Moreover, the magnitude of the acoustic mechanical work is maximum near the center of the tube since the pressure gradient and velocity amplitudes peak near the center.

Assuming that the base pressure p_0 is only a function of time, taking the spatial average of Eq. (47) yields

$$\frac{dp_0}{d\tau} = \dot{W}_{in} + (\gamma - 1)\Phi_L + (\gamma - 1)\Gamma_L, \tag{48}$$

where

$$\dot{W}_{in} = -\frac{1}{L}\int_0^L \left(\gamma \frac{\partial}{\partial x}\dot{W}_{ac}\right) dx = -\gamma \dot{W}_p,$$
$$\Phi_L = \frac{1}{L}\int_0^L \Phi dx, \quad \Gamma_L = \frac{1}{L}\int_0^L \Gamma dx. \tag{49}$$

Here, $\dot{W}_{in}$ refers to the acoustic power injected into the system by the piston and is proportional to the mechanical work done by the piston, $\dot{W}_p$. The acoustic energy injected into the system propagates towards the fixed end of the tube with the gradient of this flux increasing with the degree of nonlinearity in the system. The base heating effect is produced by the terms, $\dot{W}_{in}$ and Φ_L in Eq. (48), which are positive and increase with Knudsen number (see Fig. 16), suggesting that the rate of increase in the base pressure of the system is proportional to the Knudsen number of the system.

VI. CONCLUSION

We studied the effects of gas rarefaction on finite amplitude planar acoustic waves generated in a resonator by varying the Knudsen number over four orders of magnitude. The setup studied consisted of a piston-tube assembly with a piston oscillating at fundamental resonant frequency of the tube, closed at the other end. The tube was modeled as a one-dimensional domain neglecting the effects of shear on wave propagation. The setup was driven to a limit cycle, characterized by a balance between the resonant energy production and thermoviscous dissipation. The resonant amplification and limit cycle were simulated using the numerical discretization of the Navier-Stokes equations for low Knudsen number cases and the Boltzman equation with BGK closure for high Knudsen number cases.

The dissipation increases with the degree of rarefaction of the gas in the tube. Due to increased dissipation, the resonant response and the waveform steepening at the limit cycle is attenuated. Keeping the Reynolds number associated to the piston constant, we observed that with increasing the Knudsen number, the degree of resonance decreases, i.e., the ratio of acoustic velocity amplitude to the piston velocity amplitude decreases. Moreover, the pressure intensity profiles show that the pressure node, or the zero-crossing of the acoustic pressure tends to become quasi-stationary for very high Knudsen numbers thus suggesting that in highly rarefied gas regimes, the system behaves as a quasilinear damped oscillator even at limit cycle.

Due to an increase in dissipation with increasing Knudsen number, the smallest length scale (diffusion length scale) which exhibits acoustic energy also increases. Consequently, the acoustic wave at the limit cycle becomes less steepened with increasing Knudsen number. Since the nonlinear acoustic wave steepening entails acoustic energy cascade into higher harmonics and hence spectral broadening, the range of the acoustic energy spectrum decreases with increasing Knudsen number. We studied both the temporal and spatial spectra of the acoustic energy with varying Knudsen numbers. Furthermore, we showed that the largest harmonic or wavenumber can be estimated using the smallest length scale due to nonlinear acoustic steepening, which can be approximated by balancing the nonlinear wave propagation and dissipation terms. Scaling the spectra with the smallest length scale or timescale reveals almost exclusively sub-Kolmogorov acoustic activity for Reynolds numbers based on the maximum velocity amplitude, $\mathrm{Re}_{U_{max}}$, less than 100 and provides a quantitative metric of when to expect the formation of an inertial subrange.

At limit cycle, the energy due to resonance sustains the nonlinear waves which dissipate the energy at length scales depending on the Knudsen numbers. We showed that the dissipation of energy at the limit cycle increases the mean internal energy of the system slowly. We quantified this mean heating of the system utilizing time filtered internal energy budget equation. The results from the budget equation also reveal the scaling of dissipation with Knudsen number as Kn^2 for a fixed $\mathrm{Re}_{U_{\max}}$.

ACKNOWLEDGMENTS

The authors acknowledge the support of the National Science Foundation (NSF) Fluid Dynamics Program (Award No. 1706474) and the Air Force Office of Scientific Research (AFOSR) 2018 Young Investigator Award (YIP) (No. FA9550-18-1-0292). Computational resources are provided by the Rosen Center for Advanced Computing (RCAC) at Purdue University.

[1] W. Chester, J. Fluid Mech. **18**, 44 (1964).
[2] T. Biwa and T. Yazaki, J. Acoust. Soc. Am. **127**, 1189 (2010).
[3] C. Scalo, S. K. Lele, and L. Hesselink, J. Fluid Mech. **766**, 368 (2015).
[4] P. Gupta, G. Lodato, and C. Scalo, J. Fluid Mech. **831**, 358 (2017).
[5] T. Muir and E. Carstensen, Ultrasound Med. Biol. **6**, 345 (1980).
[6] V. F. Humphrey, in *Proceedings of the World Congress on Ultrasonics* (World Congress on Ultrasonics, 2003), pp. 73–80.
[7] V. C. B. Sousa, D. Patel, J.-B. Chapelier, V. Wartemann, A. Wagner, and C. Scalo, J. Spacecr. Rockets **56**, 319 (2019).
[8] V. Sousa, A. Batista, J. Kuehl, and C. Scalo, in *Proceedings of the 2018 Fluid Dynamics Conference* (AIAA, 2018), p. 3852.
[9] M. F. Hamilton, D. T. Blackstock *et al.*, *Nonlinear Acoustics* (Academic Press, San Diego, 1998).
[10] H. W. Liepmann and A. Roshko, *Elements of Gasdynamics* (Courier Corporation, North Chelmsford, MA, 1957).
[11] P. Gupta and C. Scalo, Phys. Rev. E **98**, 033117 (2018).
[12] T. Biwa, T. Takahashi, and T. Yazaki, J. Acoust. Soc. Am. **130**, 3558 (2011).
[13] T. Biwa, K. Sobata, S. Otake, and T. Yazaki, J. Acoust. Soc. Am. **136**, 965 (2014).
[14] D. B. Cruikshank Jr., J. Acoust. Soc. Am. **52**, 1024 (1972).
[15] S. Temkin, Phys. Fluids **11**, 960 (1968).
[16] M. Malik, T. Zang, and D. Bushnell, in *Proceedings of the 2nd International Aerospace Planes Conference* (AIAA, 1990), p. 5232.
[17] E. Reshotko, in *Proceedings of the 32nd Aerospace Science Meeting and Exhibition* (AIAA, 1994), p. 1.
[18] L. M. Mack, Boundary-layer linear stability theory, Tech. Rep. No. ADP004046, DTIC, Fort Belvoir, VA, 1984, https://apps.dtic.mil/docs/citations/ADP004046.
[19] K. Stetson, E. Thompson, J. Donaldson, and L. Siler, in *Proceedings of the 16th Fluid Plasma Dynamics Conference* (AIAA, 1984), p. 1761.
[20] M. Greenspan, J. Acoust. Soc. Am. **22**, 568 (1950).
[21] M. Greenspan, J. Acoust. Soc. Am. **28**, 644 (1956).
[22] G. Sessler, J. Acoust. Soc. Am. **38**, 974 (1965).
[23] E. Meyer and G. Sessler, Z. Phys. **149**, 15 (1957).
[24] S. Loyalka and T. Cheng, Phys. Fluids **22**, 830 (1979).
[25] W. Marques Jr., J. Acoust. Soc. Am. **106**, 3282 (1999).
[26] R. K.-H. Chu and Y. Zohar, J. Non-Equilib. Thermodyn. **23**, 195 (1998).
[27] N. G. Hadjiconstantinou and A. L. Garcia, Phys. Fluids **13**, 1040 (2001).
[28] National Bureau of Standards, J. Franklin Inst. **262**, 299 (1956).
[29] C. Cercignani, *The Boltzmann Equation and Its Applications*, Appl. Math. Sci. (Springer, New York, 1987).
[30] G. A. Bird, *Molecular Gas Dynamics and the Direct Simulation of Gas Flows* (Oxford University Press, 1994).
[31] D. A. Kopriva and J. H. Kolias, J. Comput. Phys. **125**, 244 (1996).
[32] C. Mavriplis, Comput. Meth. Appl. Mech. Eng. **116**, 77 (1994).
[33] E. F. Toro, M. Spruce, and W. Speares, Shock waves **4**, 25 (1994).
[34] P. L. Bhatnagar, E. P. Gross, and M. Krook, Phys. Rev. **94**, 511 (1954).
[35] F. Rogier and J. Schneider, Transp. Theory Stat. Phys. **23**, 313 (1994).
[36] A. V. Bobylev, A. Palczewski, and J. Schneider, C. R. Acad. Sci., Ser. I, Math. **320**, 639 (1995).
[37] C. Buet, Transp. Theory Stat. Phys. **25**, 33 (1996).
[38] L. Mieussens, J. Comput. Phys. **162**, 429 (2000).
[39] L. Pareschi and B. Perthame, Transp. Theory Stat. Phys. **25**, 369 (1996).
[40] A. V. Bobylev and S. Rjasanow, Eur. J. Mech. B Fluids **18**, 869 (1999).
[41] L. Pareschi and G. Russo, SIAM J. Numer. Anal. **37**, 1217 (2000).
[42] F. Filbet and G. Russo, J. Comput. Phys. **186**, 457 (2003).
[43] K. Nanbu, J. Phys. Soc. Jpn. **49**, 2042 (1980).
[44] H. Babovsky and H. Neunzert, Math. Methods Appl. Sci. **8**, 223 (1986).
[45] J. Davis, R. G. Dominy, J. K. Harvey, and M. N. Macrossan, J. Fluid Mech. **135**, 355 (1983).
[46] B. P. Leonard, Comput. Methods Appl. Mech. Eng. **19**, 59 (1979).
[47] A. Frezzotti, in *Proceedings of the International Symposium on Rarefied Gas Dynamics 1990: Aachen, Germany* (VCH, Weinheim, Germany, 1991), pp. 1243–1250.
[48] L. Mieussens, Math. Models Methods Appl. Sci. **10**, 1121 (2000).
[49] L. Mieussens and H. Struchtrup, Phys. Fluids **16**, 2797 (2004).
[50] S. Chigullapalli and A. Alexeenko, in *Proceedings of the 41st AIAA Fluid Dynamics Conference and Exhibition* (AIAA, 2011), p. 3993.
[51] P. Gupta and C. Scalo, in *Proceedings of the Meeting on Acoustics XXI-ISNA* (ASA, Washington, DC, 2018).